Materials Physics and Mechanics 36 (2018) 18-38 Received: November 28, 2017

DISSIPATION ENERGY DURING BRITTLE CRACK PROPAGATION IN A SINGLE CRYSTAL OF 3%SI-FE ALLOY

Tomoya Kawabata[1*], Daiki Nakanishi[1], Tetsuya Namegawa[2] and Shuji Aihara[1]

[1]The University of Tokyo, 7-3-1 Hongo, Bunkyo, Tokyo, 113-8656, Japan

[2]Nippon Steel and Sumitmo Metal Corporation, Shintomi 20-1, Futtu, Chiba 293-8511, Japan

*e-mail: kawabata@fract.t.u-tokyo.ac.jp

Abstract. Brittle fracture in carbon steel seriously impacts structural safety. It is considered that the elementary step of the brittle fracture of polycrystalline steel corresponds to cleavage in each crystal grain and their connection process. However, the detailed mechanisms of brittle fracture are not completely understood. In this study, the elementary process of brittle crack propagation is clarified using the dynamic strain recording of a strain gauge near the crack path.

The results indicate that the brittle crack propagation rate in a single crystal grain is much slower than the Rayleigh wave rate. To estimate the dissipation energy during crack propagation in a single crystal grain, dynamic finite element analyses were conducted by assuming constant critical stress during crack propagation. The dissipated energy is not small even inside a single crystal grain and appears to exhibit a proportional relationship with the stress intensity factor.

Keywords: brittle crack; steel; dissipation energy; single crystal.

1. Introduction

The problem of brittle fracture accidents in steel structures is an important issue. For example, the above- ground LNG tank that was manufactured for the first time in Cleveland (in the United States) exploded owing to the inappropriateness of material selection and welding construction prior to its full-scale operation, and it caused several fatalities. The fracture triggering point causing the accident was not clearly identified. However, it is considered that crack-like defects elongated owing to fatigue resulting from welding defects. Additionally, it is evident that the material used for the tank (low carbon 3.5% Ni alloy steel) exhibited extremely low toughness at the operating temperature of -162 °C [1]. To reliably prevent these types of accidents, standardization to prevent the occurrence of brittle fracture was promoted by utilizing a system of fracture mechanics that was developed in an extant study. However, given the seriousness of the damage, it is desirable to devise a technique to prevent complete collapse even if brittle cracks potentially occur. The process of preventing cracks during propagation is termed arrest performance, and it is required as a necessary property for steel materials used in various fields including ships, hydropower plants, nuclear power generation, and low-temperature storage tanks [2, 3, 4].

Various features in the ideal state of dynamic propagation cracks were examined by extant studies. For example, Broberg [5] shows that the stress field at the crack tip is

http://dx.doi.org/10.18720/MPM.3612018_3

described based on static state fracture mechanics. When the crack propagates in the infinite plate, the relationship between the statically calculated stress intensity factor K and the dynamic stress intensity factor K_d is expressed by Equations (1) and (2) as follows:

$$K_d = f(\beta)K \tag{1}$$

$$f(\beta) = \frac{\sqrt{1-\beta^2}R(\beta)}{\beta^2\, g_1(\beta)}. \tag{2}$$

Here:

$$\beta = \frac{V}{c_p} \tag{3}$$

$$R(\beta) = 4e^3\sqrt{1-\beta^2}\sqrt{e^2-\beta^2} - (2e^2-\beta^2)^2 \tag{4}$$

$$\begin{aligned} g_1(\beta) = {} & -4(1-\beta^2)e^2\,\mathbf{K}\left(1-\frac{\beta^2}{e^2}\right) + \left(4e^4+\beta^2(1-4e^2)\right)\mathbf{K}(1-\beta^2) \\ & + \frac{8(1-\beta^2)e^4}{\beta^2}\mathbf{E}\left(1-\frac{\beta^2}{e^2}\right) \\ & - \frac{(\beta^4+8e^4-4\beta^2(e^2+1)e^2)}{\beta^2}\mathbf{E}(1-\beta^2), \end{aligned} \tag{5}$$

where ***K*** denotes the complete elliptic integral of the first type, and ***E*** denotes the complete elliptic integral of the second type. Additionally, e denotes an elastic constant that is expressed by equation (6) as follows:

$$e = \begin{cases} \sqrt{\dfrac{1-2\nu}{2(1-\nu)}}\ (plane\ strain) \\ \sqrt{\dfrac{1-\nu}{2}}\ (plane\ stress) \end{cases} \tag{6}$$

Figure 1 shows the results that explicitly depict this relationship. The figure shows the relationship between crack propagation velocity V and dynamic stress intensity factor K_d, that is, $f(\beta)$ in equation (1) [5]. Thus, this shows that the dynamic stress field and the dynamic energy release rate are uniquely determined only if the static stress intensity factor and crack propagation rate are given. However, the steady-state crack propagation model assumes ideal elasticity, and it is assumed that the reduction in strain energy during crack propagation is uniquely determined by the crack propagation rate. However, the crack propagation of the actual material is complicated by the hierarchically contained heterogeneity as shown in Fig.2, and the stress field at the crack tip is not necessarily only determined by the apparent propagation rate as measured by experimental observation. Therefore, the present study considers the dissipated energy corresponding to each stage of the hierarchy by focusing on steel materials. In this study, the focus involved dissipation energy with respect to propagation inside a crystal grain, which corresponds to the most fundamental unit of crack propagation.

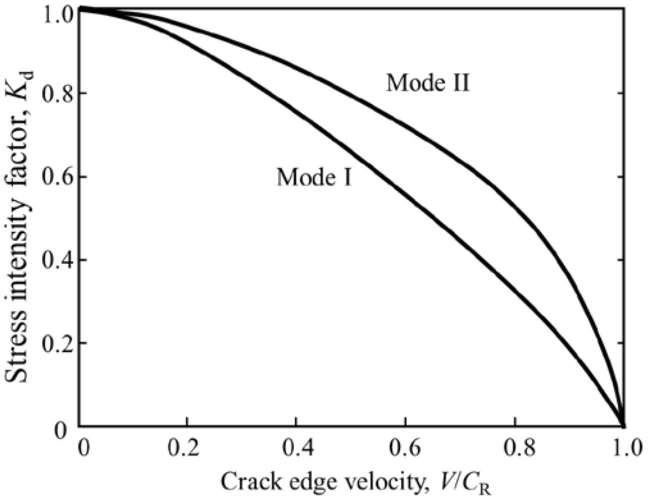

Fig. 1. Changes in the stress intensity factor by changing the crack speed [5].

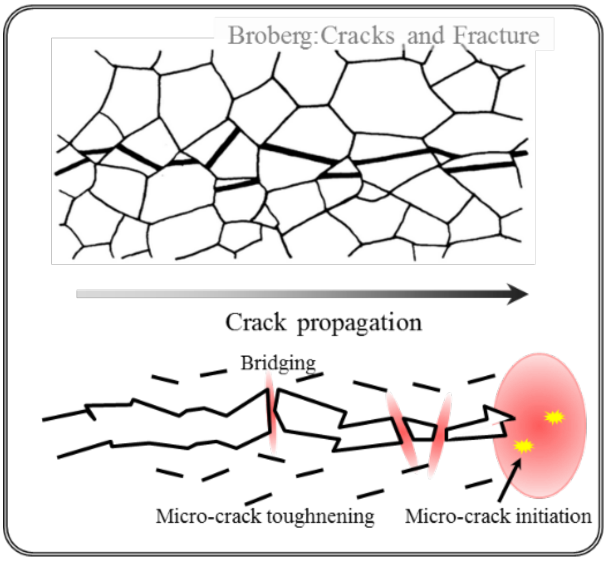

Fig. 2. Characteristics of brittle crack propagation in polycrystalline steel (modified by authors based on a picture in [5]).

As widely-known, cleavage fracture of steel materials occurs in the {100} planes. Additionally, when the fractured surfaces in the crystal grains are observed with an electron microscope, a river pattern is observed although a flat and non-characteristic region widely exists. It appears that resistance to fracture is low when we consider that irregularities on the fracture surface correspond to sources of dissipated energy. If it is possible to manufacture a steel material with extremely coarse crystal grains and measure the propagation speed in the crystal grain, then it is possible to simply predict that the propagation speed may be accelerated to the Rayleigh wave velocity given that crack branching is not considered. It is also known that the maximum propagation velocity obtained in the laboratory for steel materials approximately corresponds to 1000 m/s [6]. However, a higher propagation speed may be estimated inside a crystal grain. The upper limit value may be determined by the crack branching condition as theoretically proven by Yoffe [7] for the first time, and it approximately corresponds to 0.6 times the Rayleigh wave as confirmed by several researchers with resin materials. Thus, there was a simple expectation that the crack propagation rate is at least accelerated to this speed. There are cases of metal materials in which the crack propagation speeds approximately 0.8 times the Rayleigh wave velocity (silicon single crystal) [8] and approximately 0.6 times the Rayleigh wave velocity (tungsten single crystal) [9] were experimentally measured. However, there is a paucity of research on steel materials. In this study, to directly respond to such considerations, we fabricated a steel material with coarse crystal grains, measured the crack propagation speed in the crystal grain, and attempted to quantify its dissipation source and dissipated energy.

2. Experiment

Material used. A steel piece with the chemical composition as given in Table 1 was obtained from the test material via vacuum melting furnace-ingot production. The chemical composition contains a large amount of Si and Al that are ferrite formers, and there are no γ (f.c.c.) phases and δ (b.c.c.) phases that are stably present in common steel materials. It directly solidifies from the liquid phase to the α phase and no transformation is observed until cooling to room temperature occurs. Therefore, it is relatively easy to obtain coarse crystal grains. From the ingot, specimens were taken from various directions as shown in Fig. 3 (correspondence between the directions and marks is as shown in the figure). Furthermore, blocks for rolling were machined from the ingot, and hot rolling was performed to 16 mm of thickness. Subsequently, the temperature was increased again to 800 °C and 1300 °C to recrystallize the crystal grains. Fig.4 shows the microstructure of the material at each normalizing temperature. These materials are referred to as 2A1 and 2A2. The grain size of 2A1 is 100-300 μm and that of 2A2 is 4000-5000 μm. This steel contains only small amount of carbon, as observed in Table 1, and thus, the second phase does not exist. The material obtained under either condition is a ferrite single phase steel. The results of the tensile test and the Charpy impact test results are given in Table 2 and Table 3, respectively. It is observed that the material exhibits poor toughness at room temperature. Although the mechanical properties of the as-cast material were not investigated, it is inferred that the crystal grain size is equivalent to 2A2 and therefore, the mechanical properties are equivalent to 2A2. As shown in Fig. 5, a three-point bending specimen with a one-side notch was used. The notches were cut by electrical discharge such that the angle corresponded to 60 ° and the depth corresponded to 5 mm.

Table 1. Chemical composition of the tested material [mass%].

Material	C	Si	Mn	P	S	Al	N	O
3%Si steel	0.001	3.02	0.011	<0.002	0.0004	1.88	0.0017	<0.001

Table 2. Mechanical properties of 2A1 and 2A2.

Mark	Heat treatment		Yield stress, MPa	Tensile Strength, MPa	Elongation, %	Uniform elongation, %
	method	Temperature, °C				
2A1	normalizing	800	502	606	7.0	6.2
2A2	normalizing	1300	457	529	6.9	6.1

Round-bar, dia. 12.5 mm, G.L.=50 mm.

Table 3. Result of the Charpy impact test in 3% silicon steel.

Mark	Heat treatment, °C	Test Temperature, °C	Absorbed energy *vE*, J	Brittle area *BA*, %	Surface Transition temperature *vTrs*,°C	Energy Transition temperature *vTrE*,°C
2A1	800 normalizing	20	4	100	152	166
		80	6	99		
		150	24	93		
		200	396	0		
2A2	1,300 normalizing	20	4	100	151	156
		80	4	100		
		150	141	68		
		200	371	0		

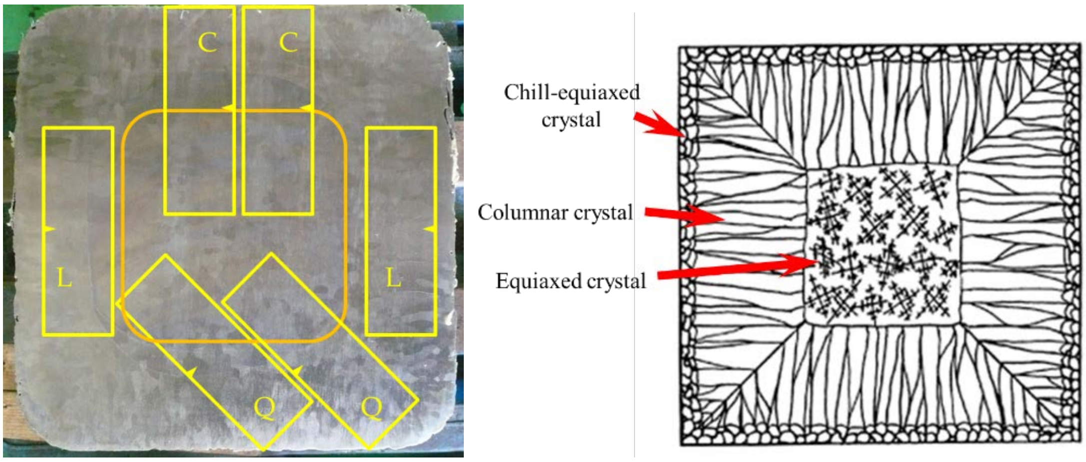

Fig. 3. Specimens in the as-cast condition.

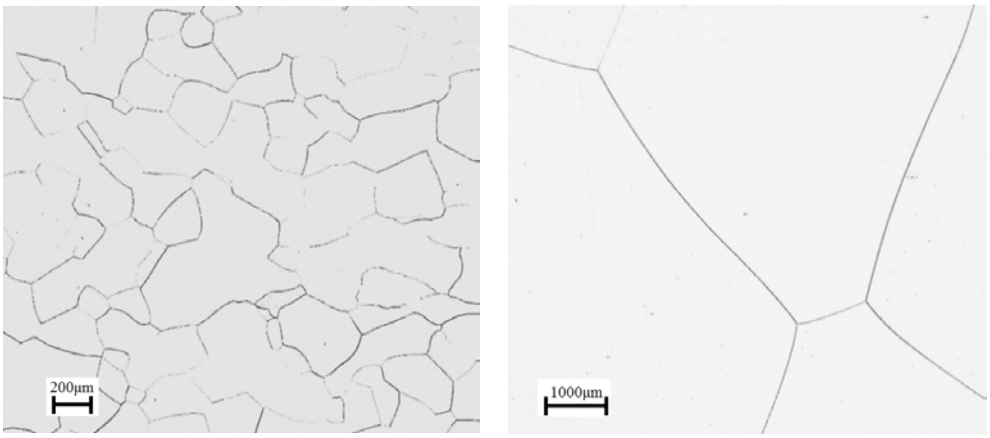

Fig. 4. Microstructure of the test materials (left: 2A1, right: 2A2).

Experiments and results. Three-point bending tests were performed at ambient temperature (20°C) and -196°C. A schematic of the test specimen setup including the jig is shown in Fig.5. We used a high-speed camera to observe the brittle crack propagation. The high-speed camera used in the test was a HPV-2A from Shimadzu Corporation in which the recordable number of shots was 102 frames and the speed of the shots was 500,000 frames per second. Additionally, the shooting time was 204 μs, which was very short, and thus, the signal of the acceleration transducer was used to trigger the recording [10]. Figure 6 shows the typical load-stroke displacement relations. When the rolled-heat-treated 2A2 was tested at room temperature, the deformation curve was smooth until the occurrence of brittle fracture. However, when it was performed at -196 °C, several small load drops were observed in the case of specimen L even at room temperature. It is estimated that this load drop during loading is not due to the occurrence of pop-in cracks but because of stress relaxation due to the large-scale twinning deformation [11]. Based on these facts, twinning deformation is likely to occur at low temperatures and a large-scale twinning deformation is more likely to occur in the as-solidified material. Furthermore, the degree of twinning deformation becomes weaker in the case of materials with fine grain.

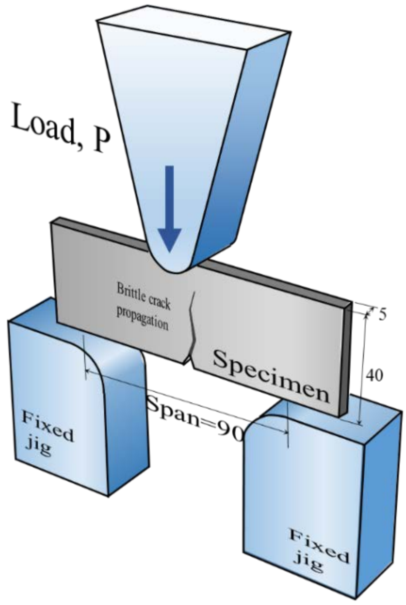

Fig. 5. Schematic of the testing set-up.

An example of a movie captured by a high-speed camera in 2A2 shows the state of the crack propagation in Fig. 7. It was confirmed that the crack propagated almost linearly within each crystal grain. The crack propagation speed observed on the surface only corresponded to approximately 300 m/s, and this was significantly lower than the propagation speed that was expected in chapter 1 ($0.6C_r \approx 1800$ m/s). Therefore, the crack propagation rate inside the specimen was evaluated by the dynamic change in the strain by the strain gauge attached to the surface. The strain gauges were bonded at the target position such that a pair of strain gauges are attached within one crystal grain for acquiring the crack propagation rate inside of the grain. The relationship between the position and the crystal grain boundary is also depicted in the photograph on the left side of Fig. 8 in which the bold line is added to clearly denote the grain boundary. The pairs in Ch.2 - 3 and Ch.4 - 5 are bonded in a single crystal grain. Table 4 presents the results of the average crack propagation velocity calculation in each section. The average value of all records was 314 m/s although it is revealed that the propagation speed exhibited significant changes according to different positions. Specifically, the crack propagation speed is the highest in the interval Ch. 4 - 5. In this interval, the results indicated that a single crystal grain also exists in the plate thickness direction, and the propagation speed in the crystal grain is significantly high when compared with the case in which it crosses the grain boundary. However, given that the Rayleigh wave velocity of steel is 2950 m/s, the crack propagation rate only corresponds to approximately half of the Rayleigh wave velocity. With respect to the interval Ch.2 - 3, the crystal grains were divided in the plate thickness direction, and it was estimated that the propagation inside the plate thickness was delayed by the grain boundary. Furthermore, the propagation speed is slowest in the interval Ch. 6 - 7. A three-dimensional measurement was conducted by using a scanning electron microscope to measure the crossing angle of each fractured facet, and the orientation difference between the grain boundaries was measured. As a summary of the result, the delayed phenomenon of propagation cracks was significant when there was a large adjacent crystal grain orientation difference including a high twist angle [10].

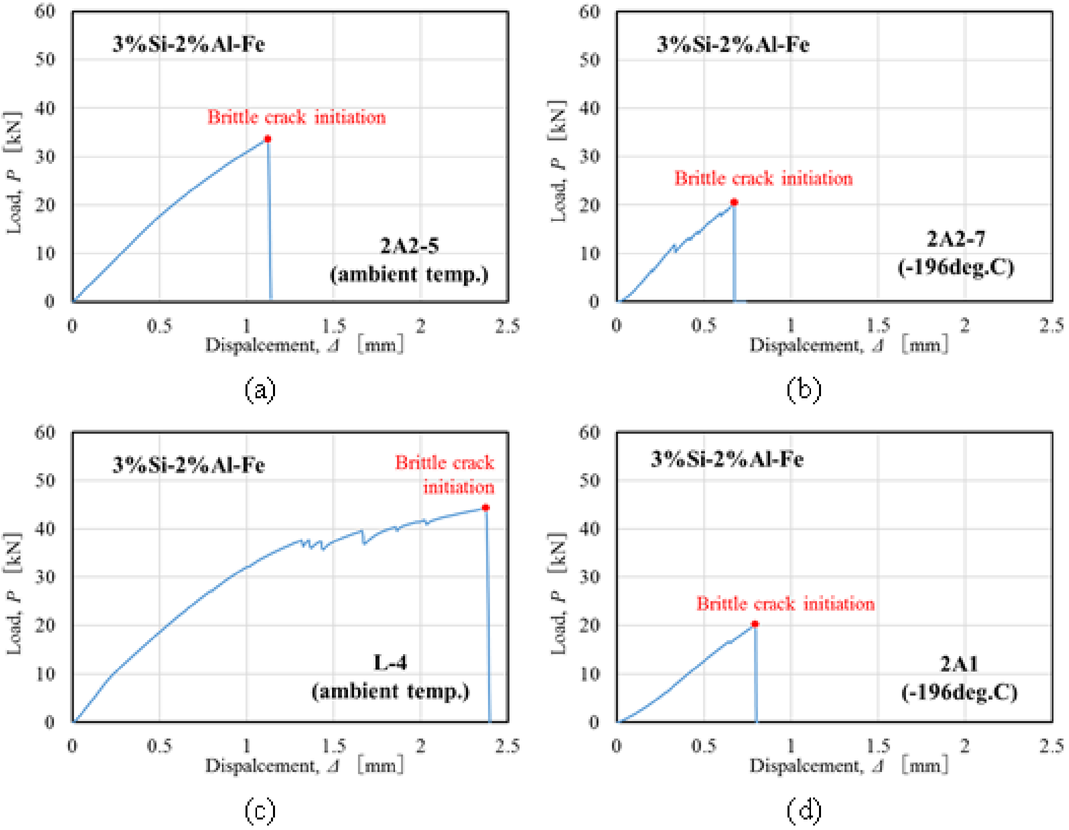

(a) (b) (c) (d)

Fig. 6. Examples of the load-displacement records of 2A2, 2A1, and L.

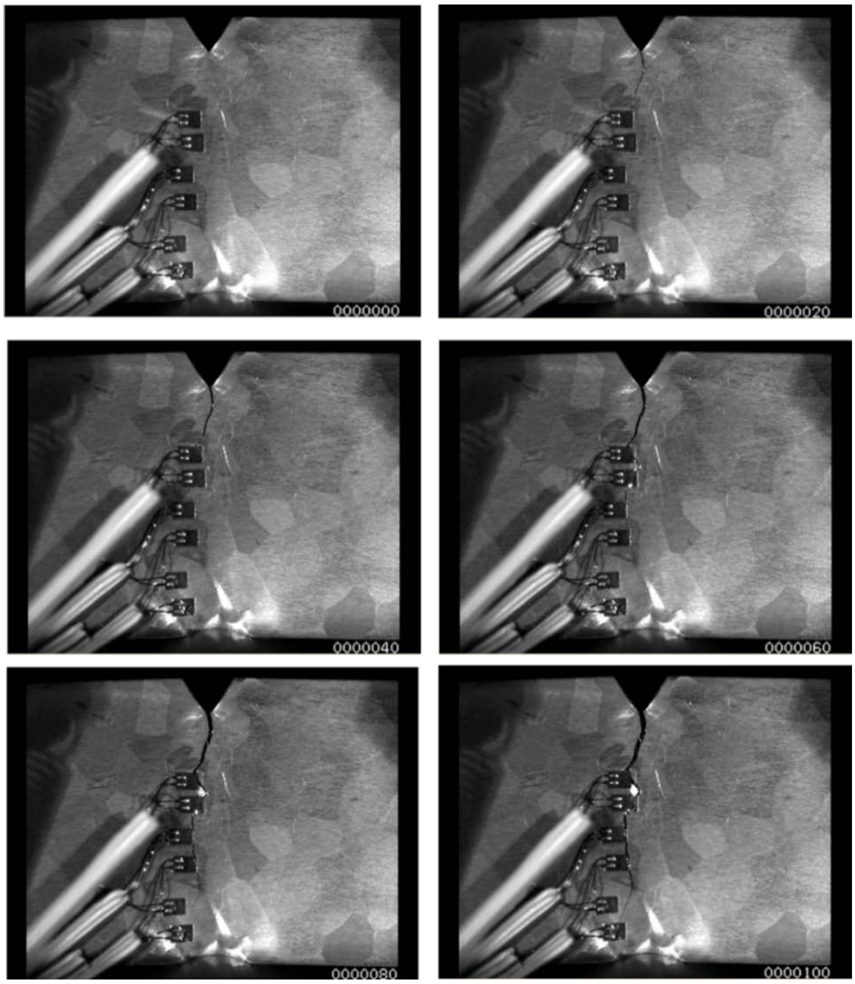

Fig. 7. High speed camera images of the frame in specimen 2A2-4 (number: time [μs]).

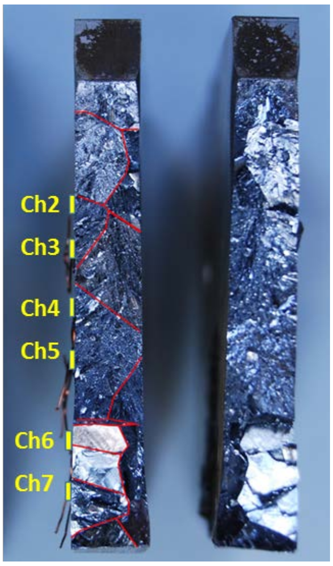

Fig. 8. Fracture appearance of 2A2-4.

Table 4. Crack propagation rate as measured by the dynamic response of the strain gauge.

Interval	Average crack speed in each interval, m/s
Ch.2~Ch.3	215
Ch.3~Ch.4	700
Ch.4~Ch.5	1447
Ch.5~Ch.6	446
Ch.6~Ch.7	127
Average	314

Microstructural factor for the relationship between crack propagation velocity and its driving force. Crack propagation rates measured with the strain gauges are organized for each microstructural feature such as the relation with steel grade and grain boundary. In this section, we first examine the approach from the continuum mechanics aspect of the stress intensity factor and the discussed crack propagation velocity. Propagation of high-speed cracks occurs under the following conditions:

$$K = K_{ID}(V,T), \tag{7}$$

where K_{ID} denotes the dynamic propagation fracture toughness and depends on the temperature crack propagation rate. Here, it is assumed that the temperature is constant. Hence, if the propagation speed increases as per Equation (1) (Fig. 1), then the driving force should decrease and the K_{ID} that is balanced according to it should also decrease. Incidentally, the relations between the crack propagation speed and the K_{ID} were experimentally evaluated in several extant studies. For example, Fig. 9 shows the rearranged results obtained by Rosakis et al. [12] in which the shadow pattern method was used to measure the crack propagation rate in 4340 steel. Given that the crack propagation velocity is the result of various physical phenomena caused by crack propagation, it is possible to provide an interpretation of the proportional relationship of K_{ID} and crack propagation velocity. Similar results were confirmed with metal materials [13] [14] and resin materials [15] [16]. It is necessary to emphasize that the relation between the propagation speed and stress intensity factor is opposite to that in Fig. 1. Although the simple explanation is difficult because the change of driving force of both is different, Sakai et al. [17] pointed out that Broberg's model calculations encounter problems in terms of consistency with actual materials. Additionally, when the stress intensity factor increases, there is no acceleration up to the Rayleigh wave, and the upper limit value of reachable propagation rate determined for each material is observed. Here, if the limit rate is denoted as V_{l}, then the crack propagation speed is generally expressed as shown in equation (8) [18]. The expression is as follows:

$$V = V_l\left(1 - \frac{K_{IA}}{K_{ID}}\right)^m, \tag{8}$$

where V_{l} denotes the limit rate, K_{IA} denotes the lower critical stress intensity factor satisfying propagation continuation determined for each specimen, and m denotes the constant.

Figure 10 shows the results of fitting the experimental results shown in Fig.9 with equation (8). In the case of V_{l} = 1500 m/s, it is observed that the expression in equation (6) can explain the result well when m=1. With respect to the relationship between the stress intensity factor and propagation rate, it is known from Kalthoff's experiment [19] that the relationship is influenced by shape, and thus, it is impossible to evaluate a unique *K*-*v* relationship between the different shapes and load types.

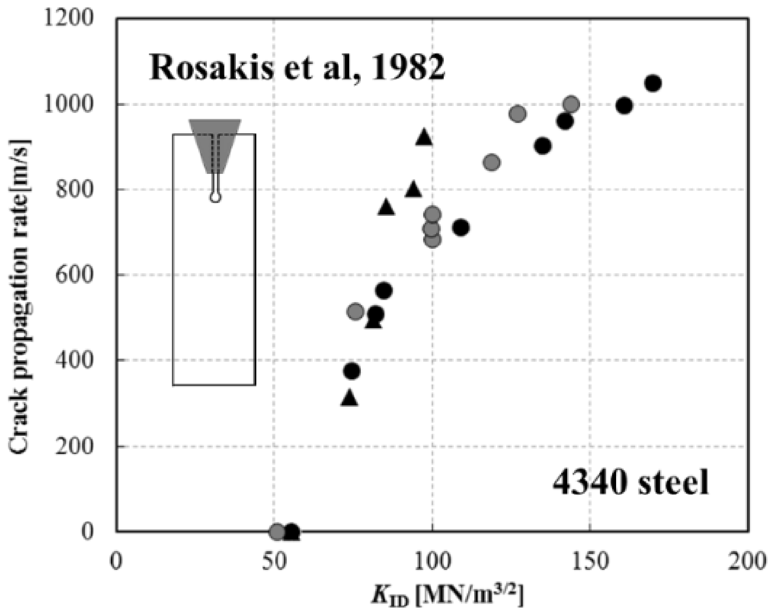

Fig. 9. Correlation between K_{ID} and the measured crack propagation rate for the experiment conducted by Rosakis [12].

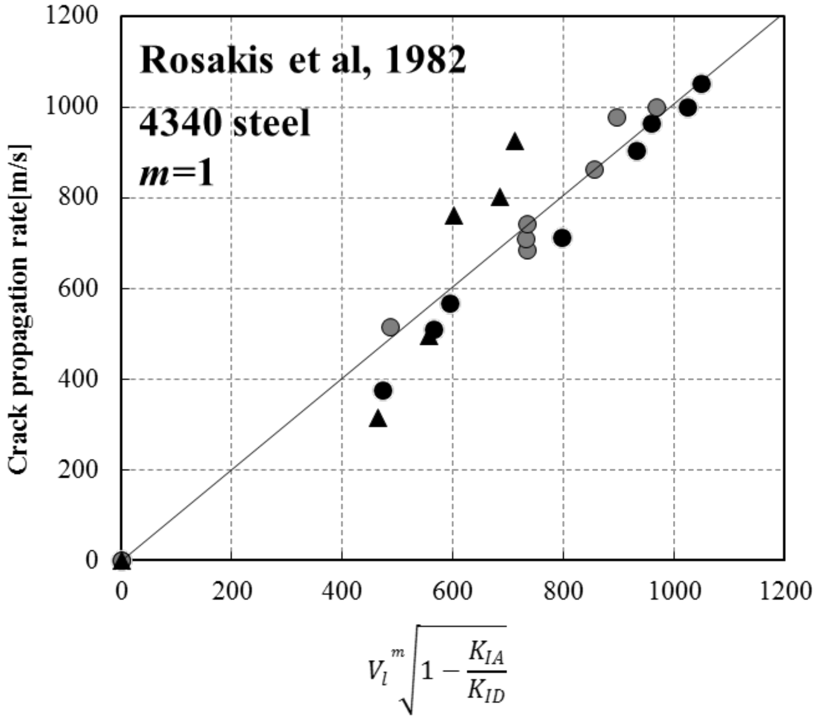

Fig. 10. Correlation between the measured crack propagation rate and its estimation for the experiment conducted by Rosakis [12].

The stress intensity factor is used to organize the test results of the study. Nevertheless, the average propagation rate of the test specimen is as low as 300 m/s, and thus a static and stress intensity factor that assumes two-dimensional elasticity is used. When the specimen is considered as an elastic body in a two-dimensional problem, it is possible to derive the driving force K value by using the following assumption [20]. It is noted that this is based on a complete equilibrium condition.

The maximum bending stress in the three-point bending test piece is represented by equation (9). The stress intensity factor is represented in two ways, namely as a function of the notch depth ratio in equations (10) and (11) [21] and as a function of the crack length as shown in equation (12). Additionally, equation (13) was obtained by setting the two equations as equal to each other. Next, we consider the energy change when the crack propagates a small amount corresponding to da. Equation (14) shows the energy release rate corresponding to the generated crack plane. Another expression for the energy release is obtained from the change in the area of the load displacement curve as shown in Fig. 6 (equation (15)). Here, $\varDelta_0$ denotes the sum of the displacement component $\varDelta_{\mathrm{no\ crack}}$ that is calculated by using beam bending theory and the displacement component $\varDelta_{\mathrm{crack}}$ due to the initial crack length (equation (16)). Each component is expressed by equations (17), (18) and (19). If both equations are equally placed and transformed, a relational expression between P and a (equation (20)) is obtained. When the expression is integrated from the initial crack length by using the arrest crack length, we obtain equation (21) that represents the load after the crack propagation. Finally, the load value is substituted into equation (12), and it is possible to obtain the stress intensity factor at an arbitrary crack length.

$$\sigma = \frac{3P_0S}{2tW^2} \tag{9}$$

$$K_1 = \sigma\sqrt{\pi a}F[a/W] \tag{10}$$

$$F[x] = \frac{1.99 - (1-x)x(2.7x^2 - 3.93x + 2.15)}{\sqrt{\pi}(1-x)^{1.5}(2x+1)} \tag{11}$$

$$K_{\mathrm{I}} = K_{\mathrm{I}}(P, a) = \frac{P}{t}k(a) \tag{12}$$

$$k(a) = \frac{3S}{2W^2}\sqrt{\pi a}F[a/W] \tag{13}$$

$$-dU = -Gtda = -\frac{K_{\mathrm{I}}^2}{E'}tda \tag{14}$$

$$-dU = \frac{1}{2}\Delta_0 dP \tag{15}$$

$$\Delta_0 = \Delta_{no\ crack} + \Delta_{crack} \tag{16}$$

$$\Delta_{no\ crack} = \frac{\sigma S^2}{6WE'} \tag{17}$$

$$\Delta_{crack} = \frac{\sigma SV(\frac{a_0}{W})}{E'} \tag{18}$$

$$V[x] = \left(\frac{x}{1-x}\right)^2(12.77x^4 - 34.94x^3 + 36.82x^2 - 19.57x + 5.58) \tag{19}$$

$$-\frac{1}{P^2}dP = \frac{2k(a)^2}{t\Delta_0E'}da \tag{20}$$

$$P = (\frac{1}{P_0} + \frac{2}{t\Delta_0E'}\int_{-a}^{a}k(a)^2da)^{-1} \tag{21}$$

Figure 11 shows the results when the crack propagation velocities are arranged at the positions between the strain gauges by using the stress intensity factor calculated by the method. The value at the midpoint of the strain gauge position was used as the stress intensity factor. As an overview, in a manner similar to Rosakis' study [12], the proportional tendency of the crack propagation rate and the stress intensity factor is clearly revealed. As explained by using the example of 2A2-4 in the previous section, the propagation speed is stratified relative to the stress intensity factor based on whether each velocity measurement interval is within a single crystal or across grain boundaries. Specifically, in this polycrystalline group, those with a large twist angle (especially at grain boundaries) exhibit an extremely low average propagation rate. This indicates the possibility of it corresponding to a delay phenomenon due to the grain boundary in a separate report of the authors [10]. Additionally, Fig. 12 shows the results of the same three-point bending test that is conducted at -125 °C and -196 °C by using general purpose 490 MPa class steel (termed as N30 [22]). Although the test temperature and the steel type are different, the same tendency is observed in the relationship between stress intensity factor and crack propagation rate. However, due to differences in strength, it was difficult to organize the same on a same graph. Thus, we rearranged this in the same manner as shown in equation (6) and Fig. 13. Given that K_{IA} is unknown from the experiment, an SIF value extrapolated to zero of the crack propagation rate was used for each microstructure group. Thus, V_l is assumed as reasonable. Additionally, m was used as a fitting parameter. However, it is assumed as only dependent on the specimen shape and load mode, and thus it was set to a constant value in this arrangement as all the tests involve the same configuration.

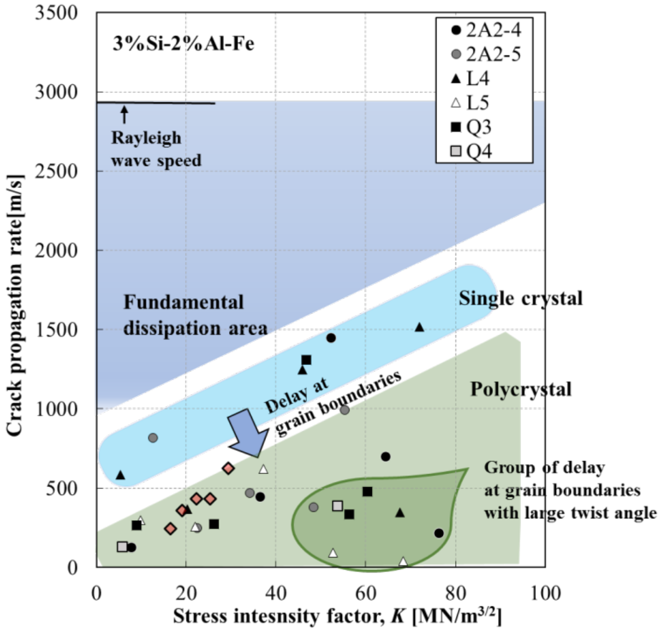

Fig. 11. Correlation of SIF and crack propagation rate in 3% silicone steel classified with respect to the microstructural features.

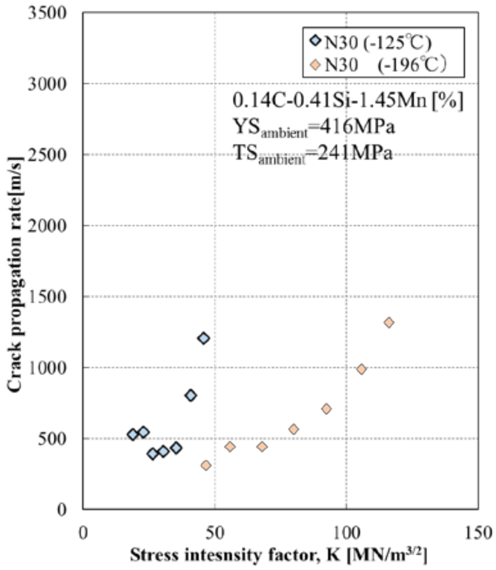

Fig. 12. Correlation of SIF and crack propagation rate in N30.

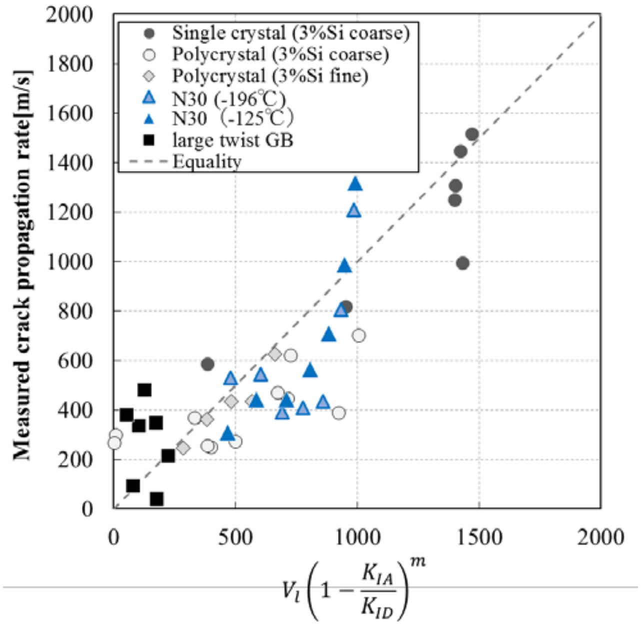

Fig. 13. Estimation of crack propagation rate by the limit speed of the material.

Table 5. Material constants for Fig. 13.

GB position	Steel	Note	V_{l}, m/s	K_{IA}, MN/m$^{3/2}$	m
Single crystal	2A2	-	1600	2	3
Polycrystal		-	1500	8	3
		Large twist GB	1000	30	3
	2A1	-	1500	7	3
	N30 (-196℃)	-	1500	6	3
	N30 (-125℃)	-	1500	15	3

Fracture surface observation inside a crystal grain. Energy dissipation due to plastic deformation at the crack tip of extremely brittle material, such as the fore-mentioned steel, appears limited, and it was assumed that the crack rate increased with increases in the stress intensity factor unless the crack branched. However, as described in the previous section, the results indicated that the crack propagation rate is remarkably slow and approximately corresponds to half the Rayleigh wave velocity even in the maximum case of a single crystal. Here we examine the characteristics of the fracture surface and consider the energy dissipation source. Figure 14 shows the fracture surface observation results of a three-point bending test. Fig.14 (a) shows the region with the highest velocity in the crystal grain, and Fig.14 (b) shows the part in which the brittle crack that propagated across the grain boundary was observed. In either case, conventional river patterns were not observed. Block patterns considered as traces of twin deformation are observed inside the crystal grain [23], and twin boundary cracks were observed in the depth direction of the fracture surface in the region in which the twin cracks intersected [24] [11]. In the grain boundary breakthrough section, a step-like difference arises owing to misorientation although all parts of the step correspond to a cleavage type [25]. Additionally, we observed the appearance of micro crack propagation and arrest at the twinned layer boundary. Both these characteristics work as resistances to the crack propagation rate of the steel and could correspond to the reason for the decrease in the crack propagation rate. Conversely, in the fine grain 2A1, the traces of twinning deformation were not completely absent but were weak. In the case of the fine-grained material, crack propagation resistance is mainly attributed to other mechanisms such as the grain boundary effect. In summary, the cause of the low rate of crack propagation in the crystal grains of 2A2 with coarse grains is considered as due to the micro-mechanisms as described above that occurred during macro crack propagation. Although a few reports observed the crack propagation behavior of the coarse single crystal materials, to the best of the authors' knowledge, previous studies were not related to the crack propagation rate.

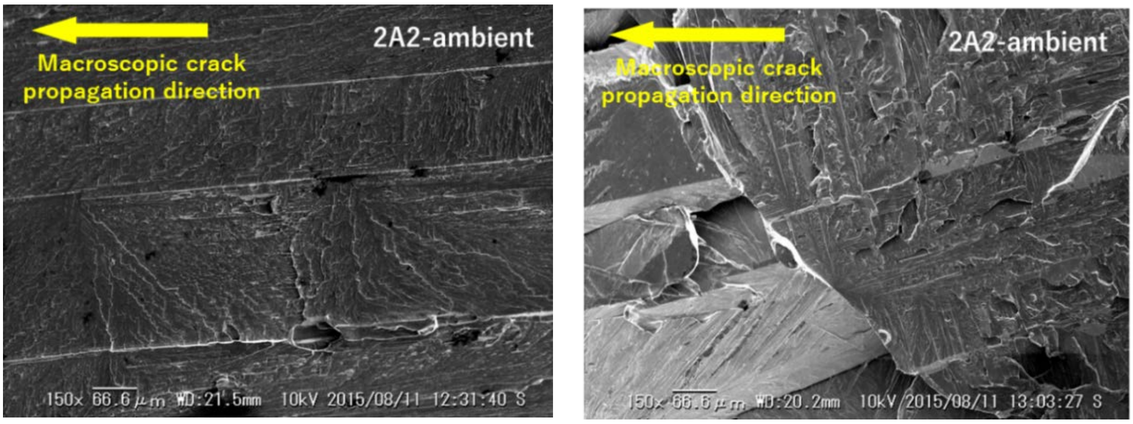

(a) Inside of grain (b) Grain boundary penetration

Fig. 14. Fracture appearance of 2A2 three-point bend specimen.

It is considered that energy dissipation micromechanisms during crack propagation are inherent in these materials, and this causes deviations from the ideal crack propagation situation. Thus, these mechanisms and their variation become a cause of the difference in crack propagation rate for the same macroscopic stress intensity factor. To predict brittle crack propagation and arresting in actual material at a practical level, it is important to clarify the dissipated energy that is inherent in material by material. Therefore, in the next chapter, a finite element method analysis using a node release method is performed to quantify the amount of energy dissipation caused by such microstructural mechanisms.

3. Quantification of energy dissipation by finite element analysis

Several extant studies demonstrate the benefits of using the finite element method for crack propagation problems. The most classical node release method [26] [27] was used for propagation analysis in this study. The method of calculation is the same as that in a recent report [28], and thus, the details are omitted. Figure 15 shows the outline of the model. The element division was finer and corresponded to 50 μm to collect detailed information about the stress and displacement distribution ahead of the crack. In the plate thickness direction, the elements were divided into five layers at equal intervals.

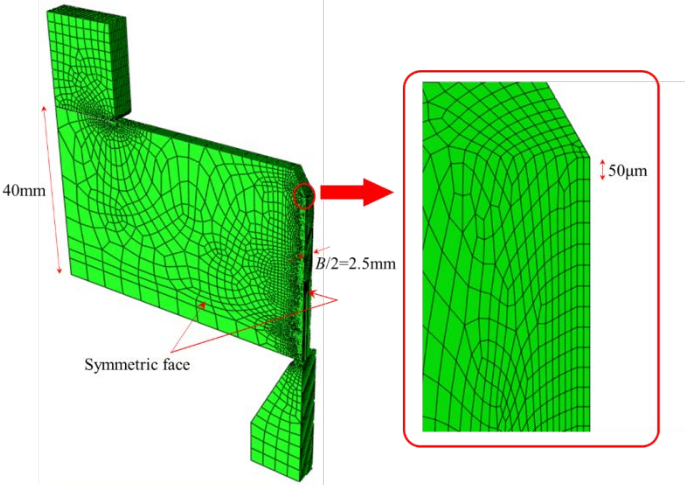

Fig. 15. FEM model outline and mesh division on the crack propagation path.

Constitutive equation of material tested. To perform calculations using the finite element method, it is necessary to clarify and input the stress strain relation including the dynamic state of the test steel. As shown in Fig.16, a strip type tensile specimen was extracted from 2A2 and strain gauges were attached to the wide portion and the narrow portion. They were used to calculate the load and strain, respectively. The displacement speed condition was changed to three levels corresponding to 0.5 mm/s, 50 mm/s, and 500 mm/s. After converting the obtained nominal stress-nominal strain relation into a true stress-true strain relation and coefficients of the Swift expression (equation (22)) and the Cowper-Symonds expression (equation (23)) [29] were determined. The results are shown in Table 6.

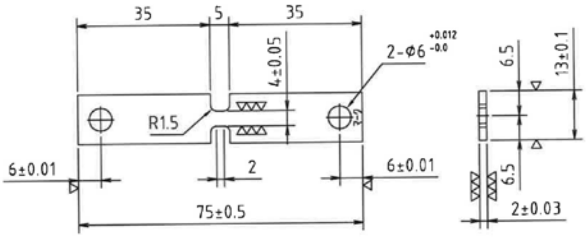

Fig. 16. Tensile specimen to determine the material constitutive equation.

$$\overline{\sigma}^{\text{static}}(\varepsilon^{\text{p}}) = \sigma_{\text{y}}\left(1+\frac{\varepsilon_{\text{p}}}{\alpha}\right)^{n} \tag{22}$$

$$\overline{\sigma}(\varepsilon^{\text{p}},\dot{\varepsilon}\,) = \overline{\sigma}^{\text{static}}(\varepsilon^{\text{p}})\cdot\left[1+\left(\frac{\dot{\varepsilon}^{\text{p}}}{C}\right)^{\frac{1}{\text{P}}}\right]. \tag{23}$$

Table 6. Coefficients corresponding to *C* and *P* in the equation.

Material	n	α	C	P	σ_{y}, MPa
3%Si (2A2)	0.0187	0.131	10000	8	480

Input data of crack propagation rate. The crack propagation speed of actual test specimen changes based on the position due to its characteristic involving a microstructural relationship with the grain boundary, and thus the crack propagation speed history of each specimen cannot be used as the input value in its original form. Therefore, the crack propagation velocity history under the assumption that the entire specimen is in the single crystal state is only extracted from the single crystal data in Fig. 11. The empirical relationship with the stress intensity factor is established as a linear function as shown in equation (24). The history of stress intensity factor from the continuum mechanics aspect viewpoint with respect to this time test piece is derived from equations (9) to (21). The calculation results of equation (12) that provide the stress intensity factor are substituted into equation (24), and the history of crack propagation rate is obtained and used for an input data of dynamic FEM analysis. Additionally, the basic process of brittle fracture of steel corresponds to stress dominant failure, and thus the constant stress value that is equivalent to the criterion is exhibited at any tip position of the dynamic propagating crack. Therefore, the crack front exhibits the tunneled shape (the crack precedes at the center of the thickness) as widely-known [30]. The tunneled shape becomes conspicuous when the driving force is strong and becomes flat when it is weak [31]. With respect to the 3% Si steel examined in this study, Qiao et al. [32] devised an arrest test to show that the arrest crack front has a tunneled shape. The expression is as follows:

$$V = 14.3K + 595 \tag{24}$$

FEM calculation results and discussions. The opening direction stress 50 μm away from the crack tip was removed and the stress at this position was assumed as the stress representing the crack driving force. The stress is termed as the characteristic distance stress. The tunneled shape of the crack was determined by trial and error by using a type of power function equation such that the characteristic distance stress is constant at the crack front at all the six node positions in the plate thickness direction (Fig. 17).

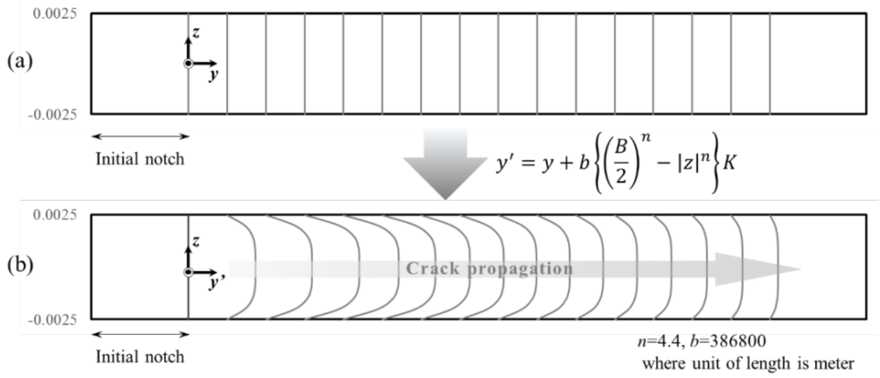

Fig. 17. Determination of the configuration of the crack front shape with respect to the average critical distance stress.

Finally, the correlation between the crack length and characteristic distance stress is obtained while assuming a flat shape crack as shown in Fig.18 (this corresponds to Fig.17(a)), and the experiment after tunnel shape trial and error is shown in Fig.19 (this corresponds to Fig.17(b)). In the case of a flat shape, the difference in characteristic distance stress is considerable, and this was resolved in the case of a suitably adjusted tunneled shape. The figures display the extent of limited crack length condition up to 28 mm where the crack propagation rate can be measured effectively. From trial and error, a substantially constant characteristic distance stress is obtained, and it is possible to consider the stress level as the critical stress of the material. In the dynamic calculation, RAMP option [33] that linearly reduces the nodal force with respect to each step time is used to suppress meaningless vibrations generated at the time when the node is released. Although this option plays a role in suppressing meaningless vibration, it is considered as corresponding to the energy dissipation of the material since it is removed from the calculation system. The energy dissipation is a component that corresponds to summation of minute energy dissipation due to the microstructural damages. The dissipated energy component, $\mathit{\Delta}E_{\mathrm{RAMP}}$, is divided by the fractured area (both area) generated for each step and is arranged as dissipated energy rate,Ω_D as shown in Fig.20. The law of conservation of energy as expressed in equation (25) is always established even during the dynamic calculation. Other terms, such as viscous dissipation in the equation of motion, are neglected here as they are very small. The expression is as follows:

$$E_W = E_K + E_U - E_{PD} - \Delta E_{RAMP}. \tag{25}$$

Here, E_W denotes the work outside of the system, E_K denotes kinetic energy, E_{W} denotes strain energy, E_{PD} denotes plastic dissipation, and ΔE_{RAMP} denotes the dissipation by the RAMP option.

The dissipated energy of the calculation for a single crystal of 3% Si alloy on an average corresponds to approximately 1500 J/m^2. Although the energy balance in the calculation is shown in Fig.21, it is ineligibly high with respect to the plastic dissipation amount. Although crack propagation occurs inside a single crystal, the crack propagation speed is not excessively high since it possesses these types of material resistance mechanisms. In the calculation result, dissipation energy somehow fluctuates. However, the decisive condition that determines the amount of dissipation energy is still unknown. This may be affected by the detailed stress state but constitutes a task to be explored in a future study.

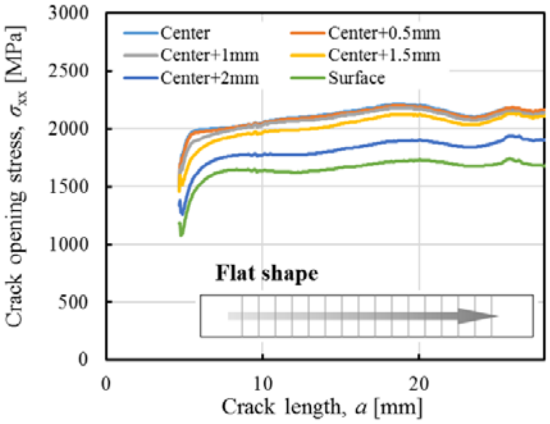

Fig. 18. History of characteristic distance stress in case of flat crack front.

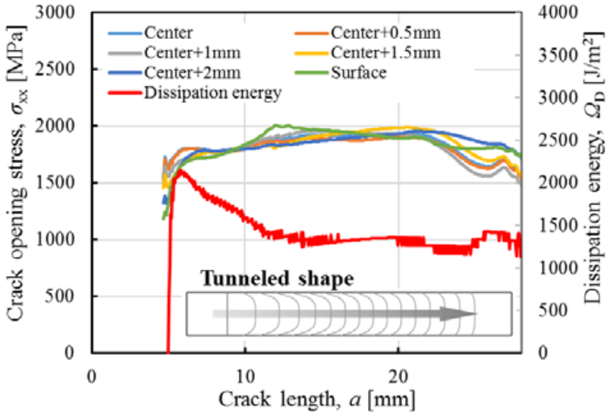

Fig. 19. History of characteristic distance stress in case of suitable tunnelled shape and calculation results of dissipation energy per unit fracture surface area.

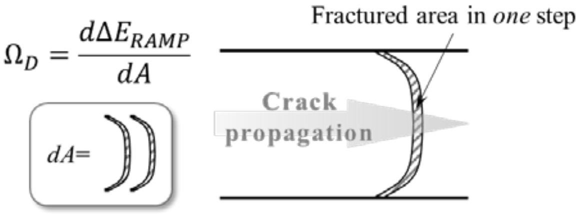

Fig. 20. Determination of other dissipation energy rates.

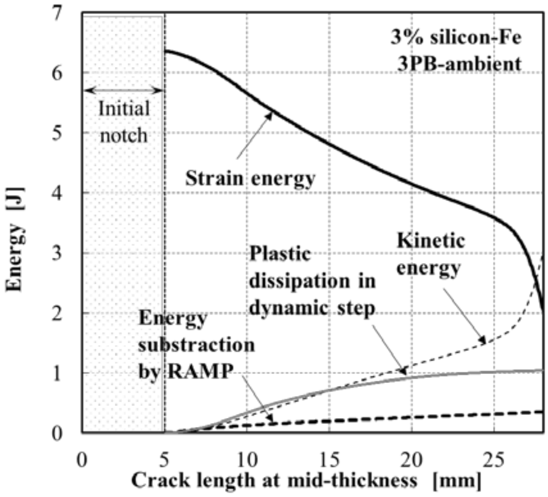

Fig. 21. Energy history during crack propagation in a virtual single crystal material.

4. Conclusions

The main objectives of this study included quantitatively obtaining the contribution of the microstructural factor in the phenomenon of brittle crack propagation and arrest in steel materials. The study first focused on the propagation phenomena in a single crystal, 3% Si containing steel with ferrite grains, and a propagation experiment and analysis were performed. The following results were obtained:

(1) To realize the propagation observation of brittle cracks within a single crystal grain (that was not observed with steel), a 3% Si-2%Al-Fe alloy with a coarse ferrite structure was manufactured. The prepared steel material was a material that was sufficiently brittle at room temperature and was suitable for observation at room temperature (for e.g., high-speed camera observation).

(2) The propagation rate was still lower than the level that is normally obtained for steel materials corresponding to an average of approximately 300 m/s. When the propagation rate inside the plate thickness was measured by the strain gauge method, the results indicated that the crack propagation speed in the section without the grain boundary was slightly higher. The crack propagation rate in the part that includes the grain boundaries is low. However, the crack propagation rate is extremely low in the part that contains a high twist angle in the mis-orientation of the grain boundaries.

(3) The crack propagation rate increases with increases in the stress intensity factor. This is consistent with the results of extant experimental investigations. The findings revealed that an empirical formula could be formulated by appropriately assuming that the reaching limit speed and other material parameters were constant. The formula uniquely depicts the relationship between the propagation speed and the stress intensity factor beyond the steel type.

(4) The results from the observation of the fracture surface indicate that it is the fracture surface property that is significantly affected by the twinning deformation generated prior to the crack tip arrival. Additionally, the roughness of the fracture surface is high and includes the generation of twin boundary cracks from the intersection of the twinning deformation layer. Moreover, the observations indicated low twinning deformation in the case of a material with a fine crystal grain size and traces of twinning deformation.

(5) In an ideal elastic model, such as Broberg’s solution, the relationship between the stress intensity factor and the crack propagation velocity are inversely proportional to each other.

However, the experimental results show that this is proportional. This is owing to the change in energy dissipation caused by the material with changes in the stress intensity factor. This is validated by the calculated history of energy dissipation in which a crack propagates in a single crystal in the devised FEM analysis with the optimization of the crack front shape such that the characteristic distance stress is constant. Furthermore, the amount approximately corresponds to 1500 J/m^2. The dissipated energy is ineligibly high when compared to the plastic dissipation generated in FEM analysis. This could be the reason as to why the measured crack propagation rate is significantly lower than the theoretically obtained value.

***Acknowledgements**. The authors wish to acknowledge ISIJ Innovative Program for Advanced Technology for financial support and dedicated discussions of this study.*

References

[1] Atallah, *Firehouse*, 1979
[2] BS EN 14620-1:2006.
[3] WES3003, *Japanese Welding Engineering Society,* 1995.
[4] API RP 579-1, ASME FFS-1, *American Petroleum Institute,* Fitness-For-Service, Third Edition.
[5] K. Bertram Broberg, *Cracks and Fracture* (Academic Press, 1999).
[6] J. J. Gilman // *Journal of Applied Physics* **27(11)** (1956) 1262.
[7] E.H Yoffe // *Philosophical Magazine* **42**(1951) 739.
[8] T. Cramer et al // *Physical Review Letters* **85(4 24)** (2000) 788.
[9] D. Hull, P. Beardmore // *International Journal of Fracture Mechanics* **2(2)** (1966) 468.
[10] D. Nakanishi, T.Kawabata and S. Aihara // *Acta Materialia*, submitted.
[11] F. Terasaki // *Japan Metallurgical Society bulletin* **9(3)** (1970) 147.
[12] A. J. Rosakis and L. B. Freund // *Journal of Engineering and Material Technology,* **104(2)** 115.
[13] J. Eftis and J.M.Krafft // *Journal of Basic Engineering* **87(1)** 257.
[14] T.Kanazawa and S.Machida, In: *Fracture Torelence Evaluation*, ed. by T. Kanazawa, A.S. Kobayashi and K.Iida (Toyo print, Japan, 1982).
[15] T.L. Paxton and R.A. Lucas, In: *Dynamic Crack Propagation*, ed. by G.C. Sih (Noordhoff, Leyden, 1973), p.415.
[16] A.S. Kobayashi and S. Mall // *Experimental Mechanics* **18(1)** (1978) 11.
[17] Y. Sakai // *JHPI* **21(2)** (1983) 95.
[18] M.F.Kannin and C.H.Popelar, In: *Advanced Fracture Mechanics* (Oxford Engineering Science Series).
[19] J.F. Kalthoff, In: *The proceedings of the NSF-ARO Workshop on Dynamic fracture,* ed. by W.G.Knauss, K. Ravi-Chandar and A.J.Rosakis (1983), p.11.
[20] T. Anderson, *Fracture Mechanics - Fundamentals and Applications* (CRC Press, 2005), third edition.
[21] H. Tada, P.C. Paris and G.R. Irwin, *The Stress Analysis of Cracks Handbook* (ASME Press, 2000), 3rd edition.
[22] T. Kawabata, T. Namegawa, M. Kaneko, Y. Shimada, H. Tajika, K. Shibanuma and S. Aihara, *Proceedings of the twenty-fifth(2015) International Offshore and Polar Engineering Conference* (Hawaii, USA), Vol.4.
[23] K. Tsujii, M. Tanaka, K. Higashida, M. Fujikura and K. Ushioda, *Dislocations2012,* (Budapest, Proceedings).
[24] F. Sorbello, P.E.J. Flewitt, G. Smith and A.G. Crocker // *Acta Materialia* **57** (2009) 2646.

[25] Y. Qiao, AS. Argon // *Mechanics of Materials* **35** (2003) 313.

[26] A.S. Kobayashi, A.F. Emery and F. Mall, In: *Fast Fracture and Crack Arrest*, ASTM STP627, ed. by G.T. Hahn and M.F. Kanninen (American Society for Testing and Materials, Philadelphia).

[27] G. Yagawa, Y. Sakai and Y. Ando, In: *ASTM STP 627*, ed. by G.T. Hahn and M.F. Kanninen (1976).

[28] T. Kawabata, Y. Nishizono and S. Aihara // *Theoretical and Applied Fracture Mechanics*, Accepted, in press.

[29] G.R. Cowper and P.S. Symonds, In: *Brown University, Division of Applied Mathematics report* (1957).

[30] G.M. Boyd // *Engineering* **16** (1953) 65.

[31] T. Kawabata and S. Aihara // *Journal of the Japan Society of Naval Architects and Ocean Engineers* **21** (2015) 63.

[32] Y. Qiao and A.S. Argon // *Mechanics and Materials* (2003) 129.

[33] SIMULIA Abaqus v.6.14.1